Table of Contents

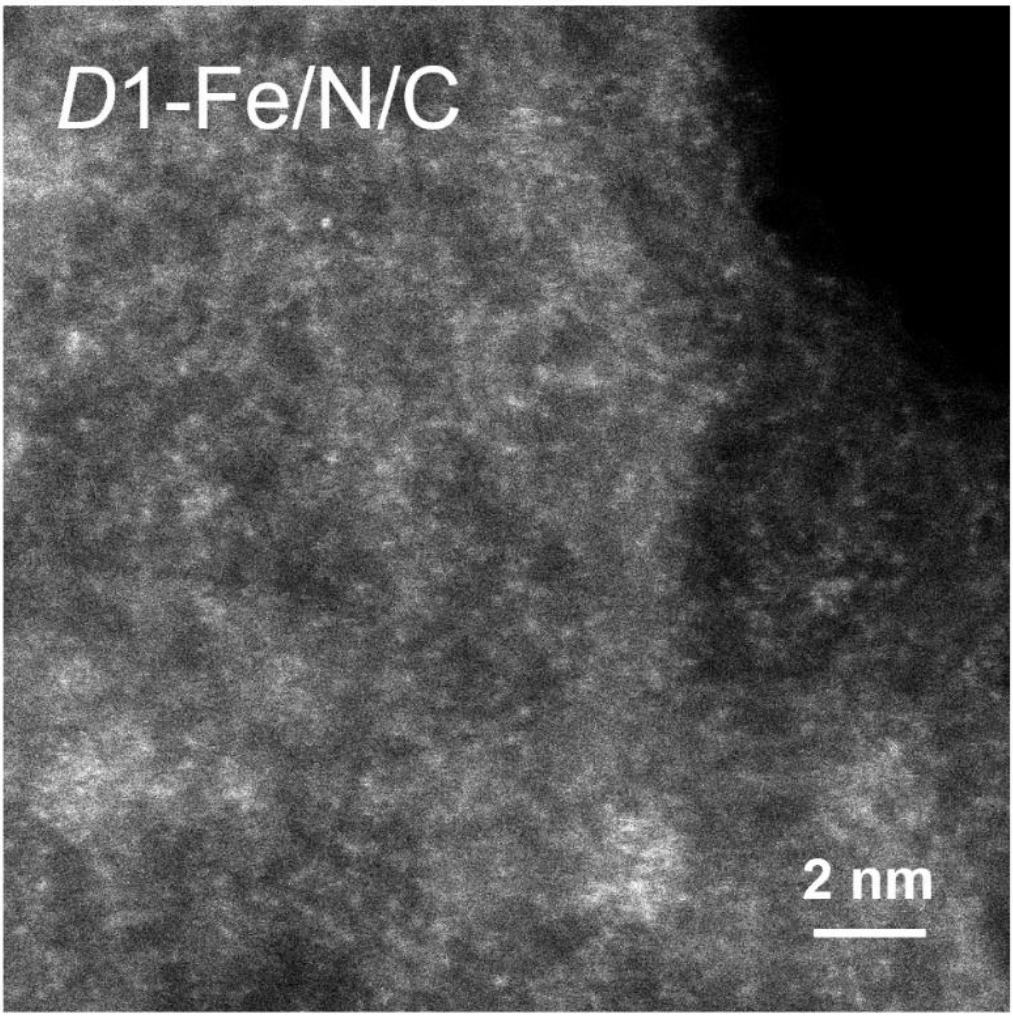

Supplementary Fig. 1. HAADF-STEM images. The catalyst shown in the picture is *D*1-Fe/N/C. HAADF-STEM did not detect Fe aggregation, indicating that Fe exists in a single-atom state in *D*1-Fe/N/C.

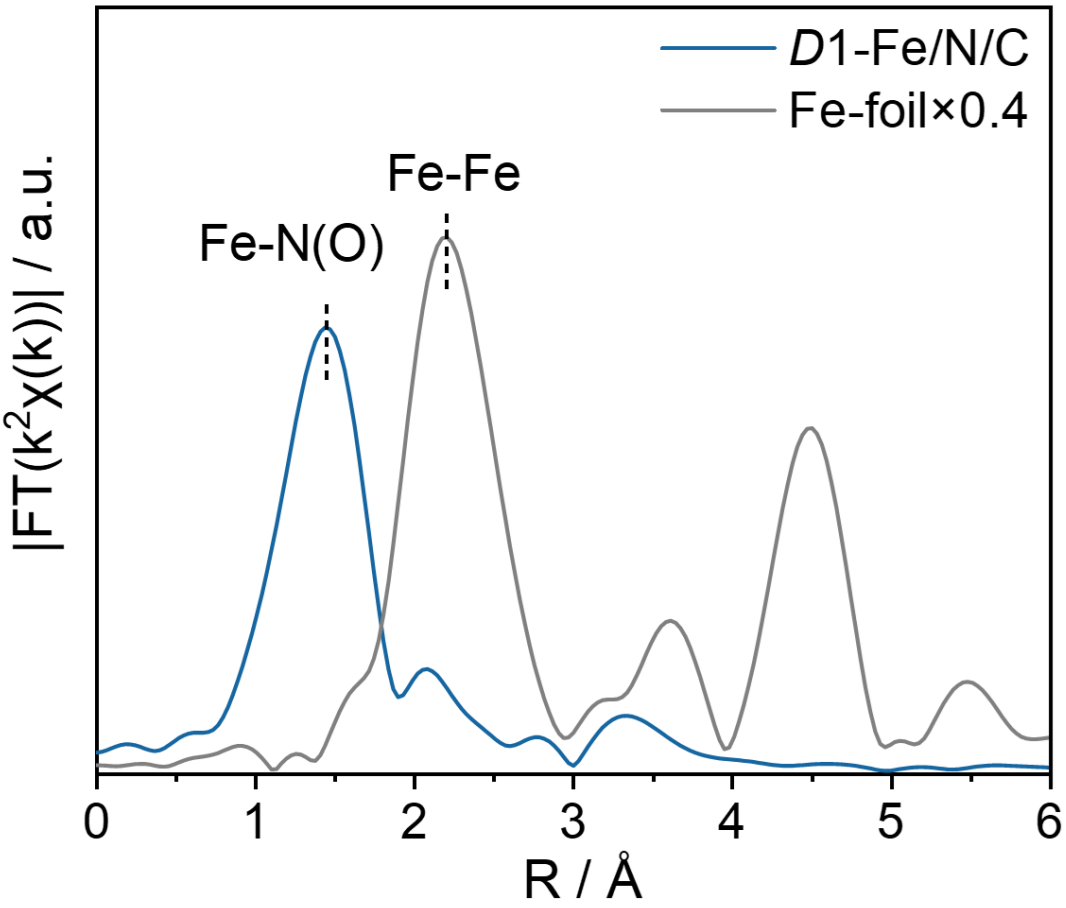

Supplementary Fig. 2. K-edge FT-EXAFS. The spectrum of the *D*1-Fe/N/C was shown with Fe foil as reference. The Fe foil spectrum is shown at 40% of the original intensity.

The main peak in the FT-EXAFS spectrum is at 1.44 Å, corresponding to Fe-N(O), and no Fe-Fe bond was observed at 2.2 Å, supporting the single-atom dispersed form of Fe sites.

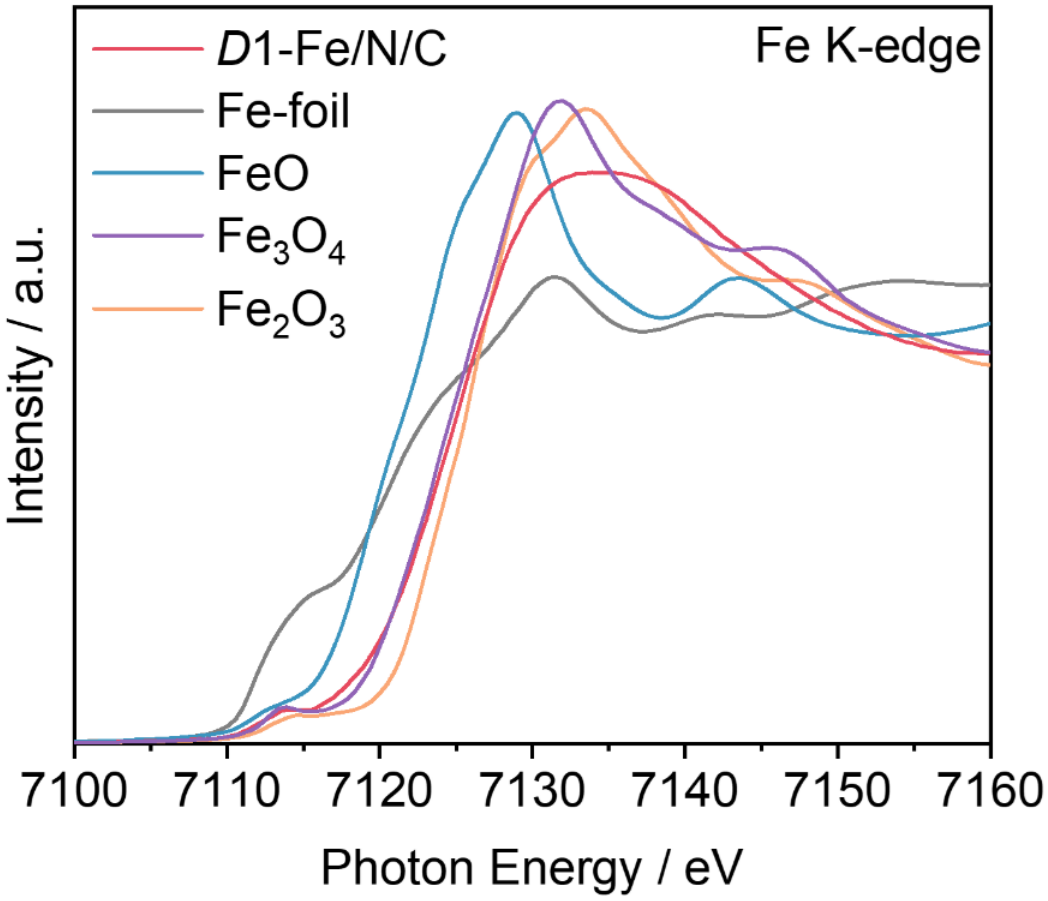

Supplementary Fig. 3. Fe K-edge XANES spectra. The spectrum of *D*1-Fe/N/C was shown with Fe foil, FeO, Fe_3O_4 and Fe_2O_3 as the reference.

The XANES of Fe K-edge in *D*1-Fe/N/C shows that its absorption edge lies between the reference peaks of Fe_3O_4 and Fe_2O_3, and is closer to Fe_3O_4. This indicates that the average oxidation state results from the presence of a mixture of Fe^{2+} and Fe^{3+} species.

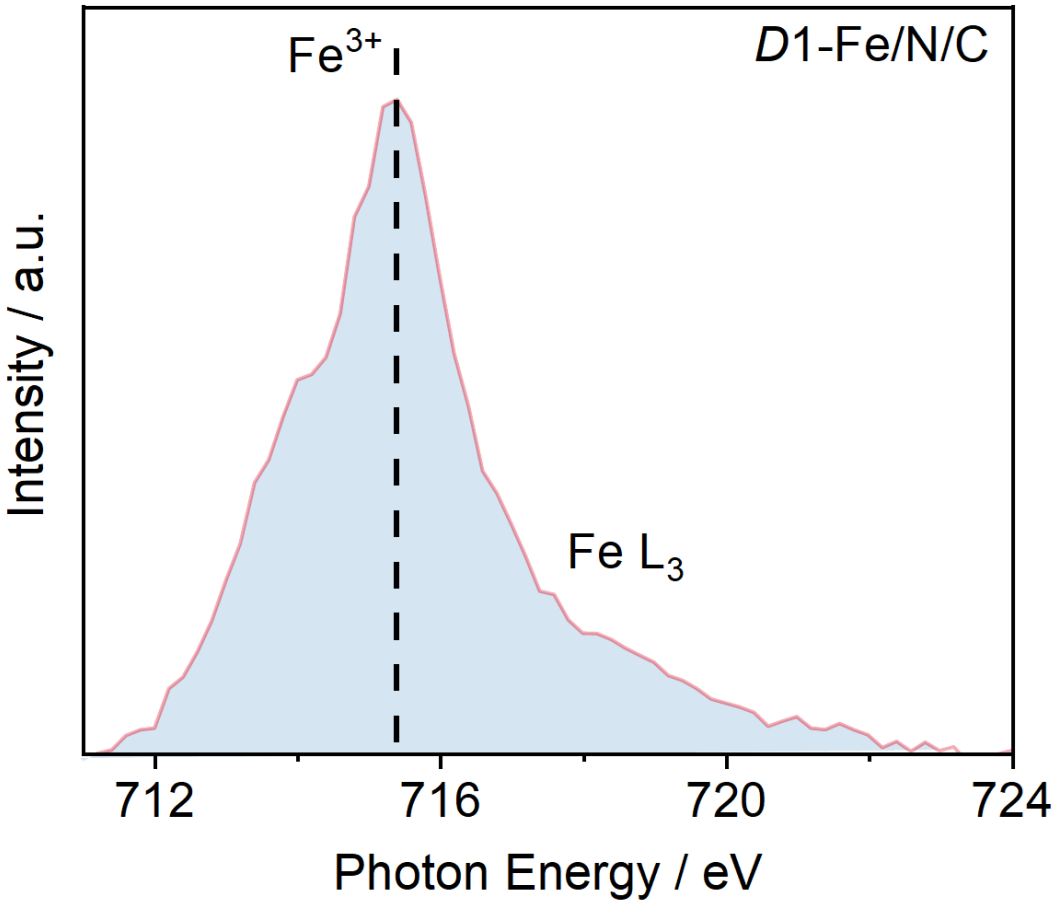

Supplementary Fig. 4. Fe L_{III}-edge XANES spectrum of *D*1-Fe/N/C.

The primary peak observed at 715.4 eV is characteristic of Fe^{3+}, confirming that Fe^{3+} is the predominant species while Fe^{2+} constitutes only a minor fraction in the *D*1-Fe/N/C catalyst.

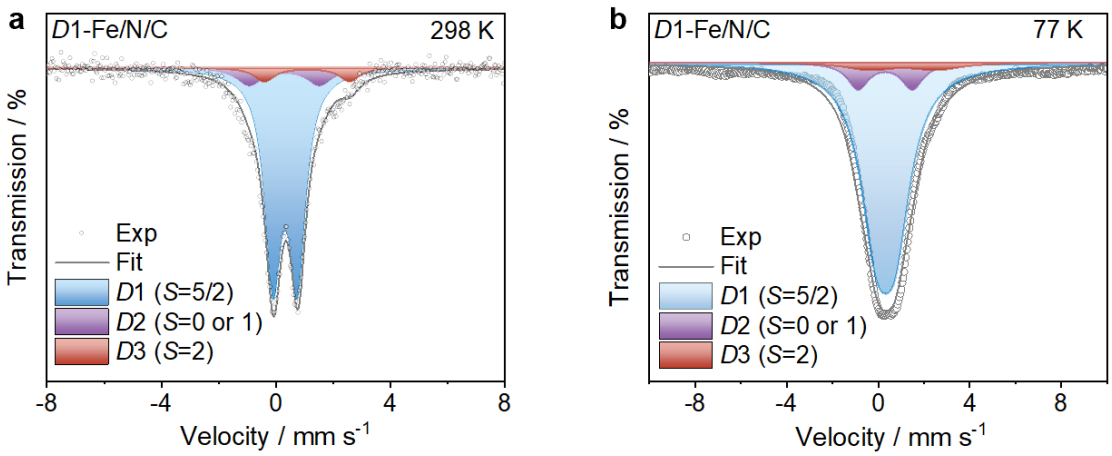

Supplementary Fig. 5. Mössbauer spectra. ^{57}Fe-labeled *D*1-Fe/N/C powder Mössbauer spectra recorded at **a**, 298 K and **b**, 77K.

In the Mössbauer spectrum of *D*1-Fe/N/C at both temperatures, Fe is divided into three states: *D*1, *D*2, and *D*3, and no sextuplets of magnetic Fe species were observed. The *D*1 state accounts for 82% of the total single-atom sites.

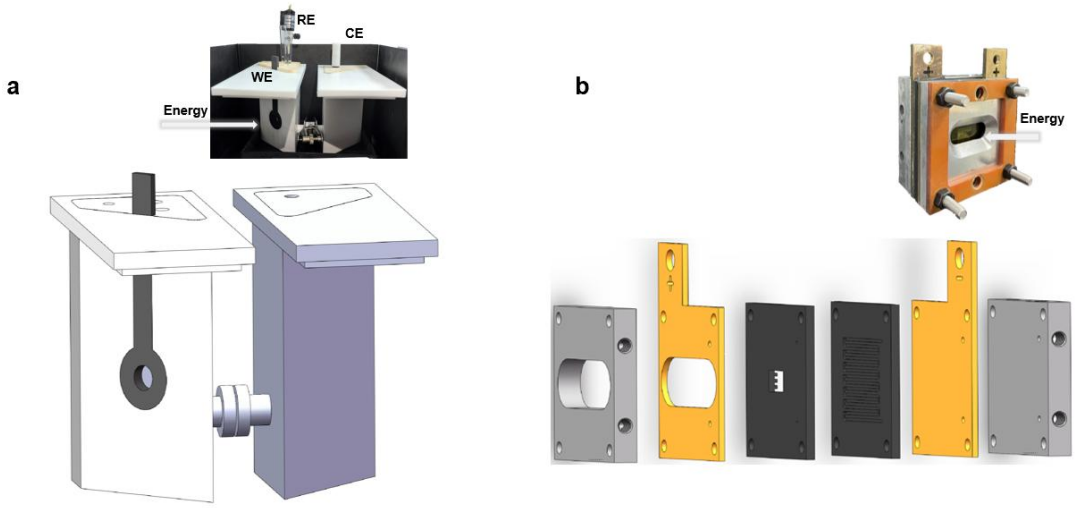

Supplementary Fig. 6. Experimental setups. Schematic diagram of **a**, H-Cell and **b**, MEA. The insert in the upper right corner of each diagram shows the corresponding photograph of each experimental setup.

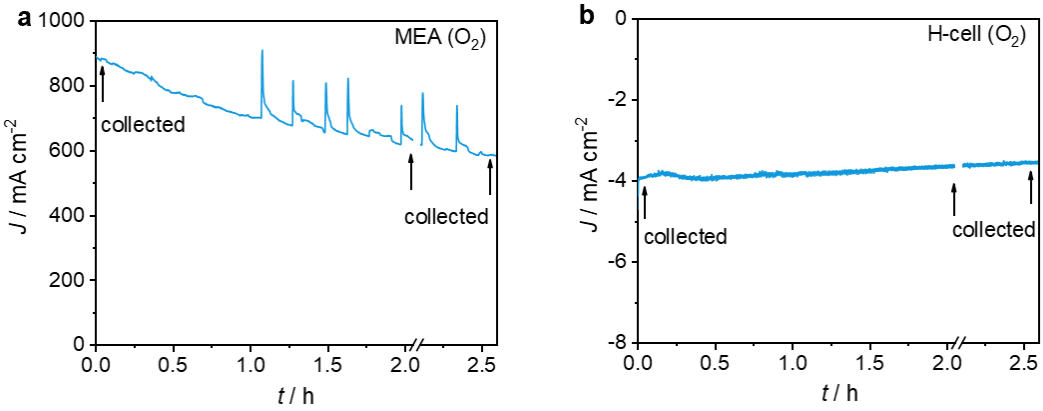

Supplementary Fig. 7. Plots of stability curves. a, I-t curves in MEA under O_2 at a cell voltage of 0.5 V. Test conditions: 0 bar back pressure, 80 °C of cell temperature, with the cathode supplied with humidified O_2 at a flow rate of 0.6 L min^{-1}, and the anode supplied with humidified H_2 at a flow rate of 0.3 L min^{-1}. The gas humidification temperature was maintained at 80°C. **b,** I-t curves in H-cell at a cathode potential of 0.5 V_{RHE}. Test conditions: 0.1 M $HClO_4$ electrolyte using saturated O_2, SCE is used as the RE and graphite is used as the CE, the two chambers of the anode and cathode are separated by Nafion 211 membrane.

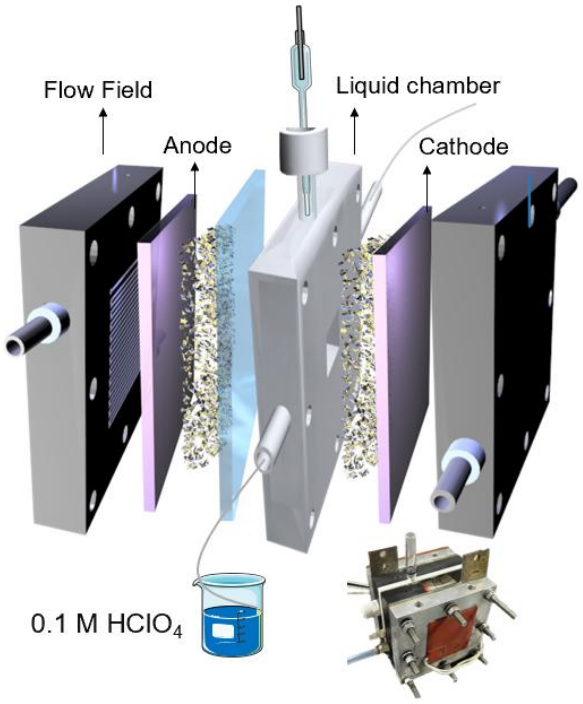

Supplementary Fig. 8. Experimental setup of flow cell. Installation diagram for GDE-based flow cell. The corresponding illustration (in the bottom right corner) presents the relevant photograph of the experimental setup.

The electrolyte flows through the liquid chamber, while the gas flows through the graphitic flow field. The reference electrode is placed in the liquid chamber to contact the flowing electrolyte during the electrochemical tests.

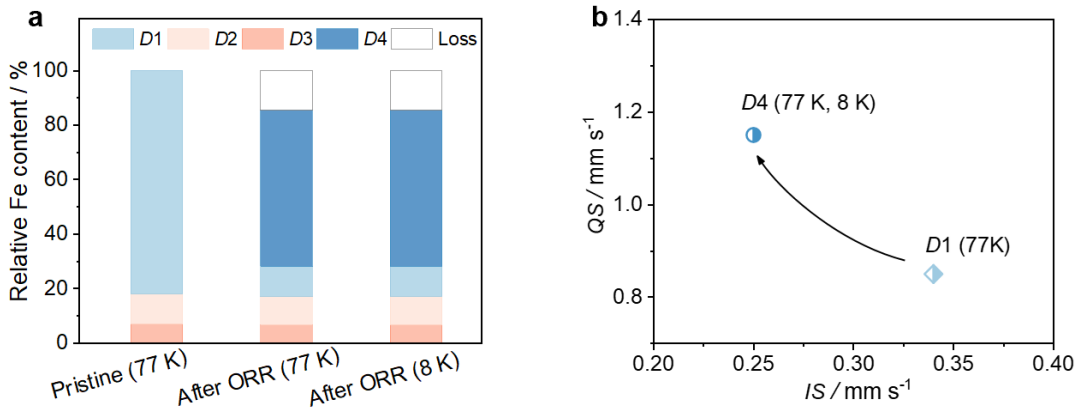

Supplementary Fig. 9. Postmortem Mössbauer spectroscopy. a, Relative abundance of different Fe species before and after the ORR at 77 K and 8 K. After ORR, the Fe content in the cathode was determined to be 84% of the pristine value. Based on the component ratios obtained from Mössbauer spectral fitting, the relative abundances of the individual Fe species were further quantified by multiplying by 0.84 the RA (%) after ORR reported in Table S1. **b,** Comparison of *QS* and *IS* parameters between the *D*1 and *D*4 states.

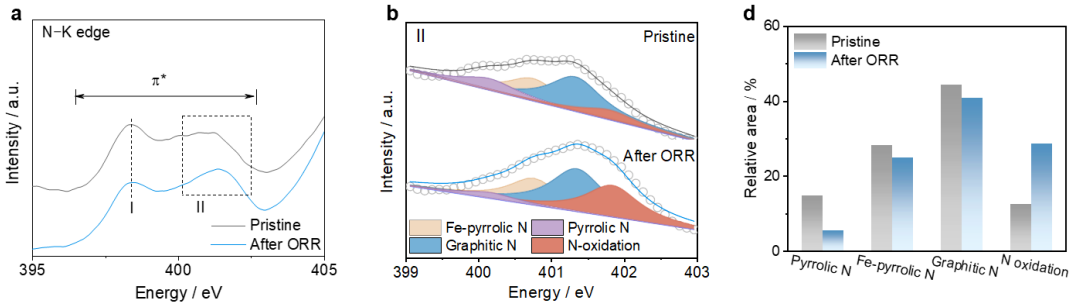

Supplementary Fig. 10. Postmortem soft K-edge XANES. a, N K-edge XANES of the GDE for the pristine catalyst and after ORR. **b**, Peak deconvolution of N-K edge XANES at 399-403 eV. **c**, Relative content of four different N species in the GDE for the pristine catalyst and after ORR.

The absorption signals in the 396-403 eV range are attributed to $N_{1s} \rightarrow \pi^*$ transitions[1, 2]. In this region, the peak at 398.4 eV is assigned to pyridinic N (Peak I)[3, 4], while the broad feature from 399-403 eV (Peak II) originates from multiple N species. While Peak I maintains its energy position, Peaks II show a minor shift. Deconvolution of Peak II identifies four N configurations: pyrrolic N (400.0 eV), Fe-coordinated N (400.7 eV), graphitic N (401.3 eV), and oxidized-N (401.8 eV)[5, 6]. Quantitative analysis reveals that pyrrolic N decreases from 14.8% to 5.5%, Fe-pyrrolic N from 28.3% to 25%, graphitic N from 44.4% to 40.9%, while N-O species increased from 12.5% to 28.6%. These results show that N oxidation occurred mainly at the pyrrolic N sites.

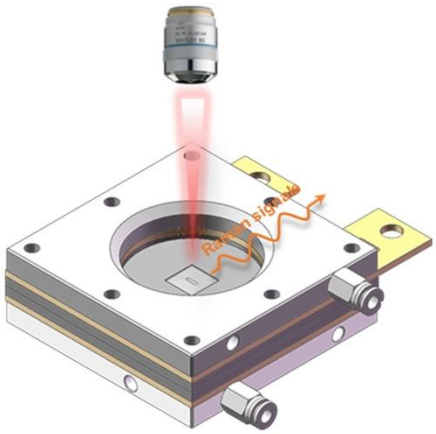

Supplementary Fig. 11. Schematic diagram of *operando* Raman device. The graphite plate was windowed and sealed with a quartz window to simultaneously maintain gas tightness and the integrity of the flow field.

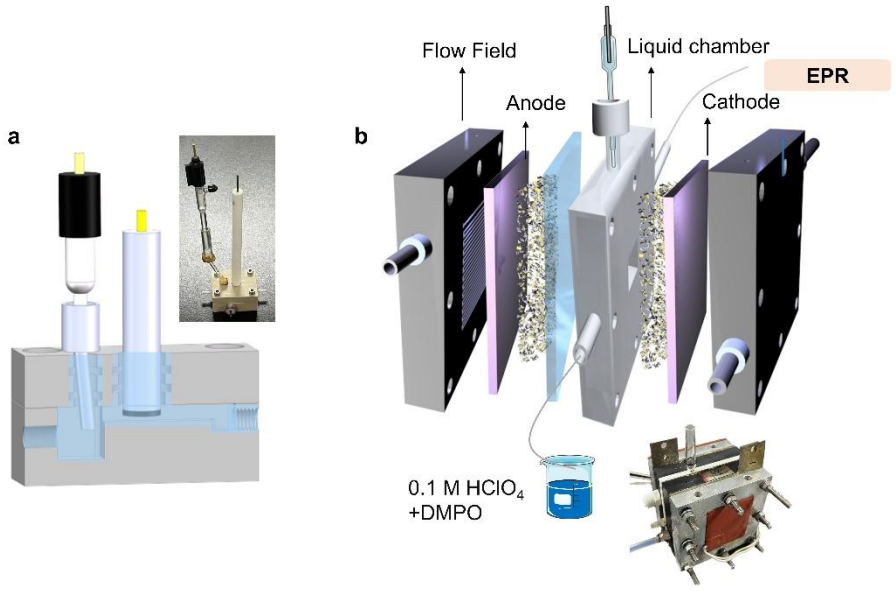

Supplementary Fig. 12. Diagrams of *on-line* EPR device. **a**, *On-line* EPR equipment on the RDE level consists of a salt bridge (coupled with RE), WE and CE. Below is a cross-sectional view of the cell. The electrolyte layer below the working electrode is controlled to 1 mm thickness and the fluid flow direction is from left to right. The photograph of the experimental device is shown in the upper right corner. **b,** *On-line* EPR equipment on the GDE level. The GDE-based flow cell consists of symmetric graphite gas flow fields and GDEs, with the cathode and anode compartments separated by a membrane. An additional PTFE liquid flow plate is positioned adjacent to the cathode side. This PTFE plate incorporates inlet and outlet channels for electrolyte circulation and integrates a salt bridge. The inset in the lower right corner is a photograph of the experimental device.

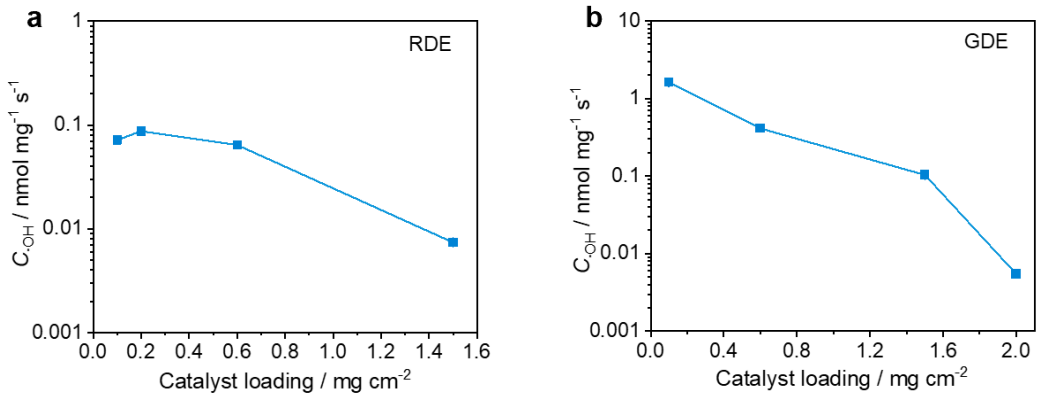

Supplementary Fig. 13. Radical generation at different catalyst loadings. a, Radical concentrations measured at 0.2 V_{RHE} in a RDE setup with various catalyst loadings of 0.1, 0.2, 0.6, and 1.5 mg cm^{-2}. **b**, Radical concentrations measured at 0.2 V_{RHE} in a GDE flow cell with various catalyst loadings of 0.1, 0.6, 1.5, and 2.0 mg cm^{-2}. The measurements were performed using a circulating 0.1 M $HClO_4$ solution containing 3 vol. % DMPO of radical scavenger, maintained at a volumetric flow rate of 1.5 mL min^{-1}.

Online EPR spectroscopy was employed to monitor radical species under varying catalyst loadings to determine the optimal experimental conditions. In the RDE configuration, the radical signal intensifies as the loading decreases, eventually leveling off at lower loadings. Conversely, a monotonic increase in radical concentration is observed in the system across the loading range from 2.0 down to 0.1 mg cm^{-2}. One possible reason lies in that, even at a low loading of 0.1 mg cm^{-2} in the GDE, there remains a portion of the catalyst that is not utilized.

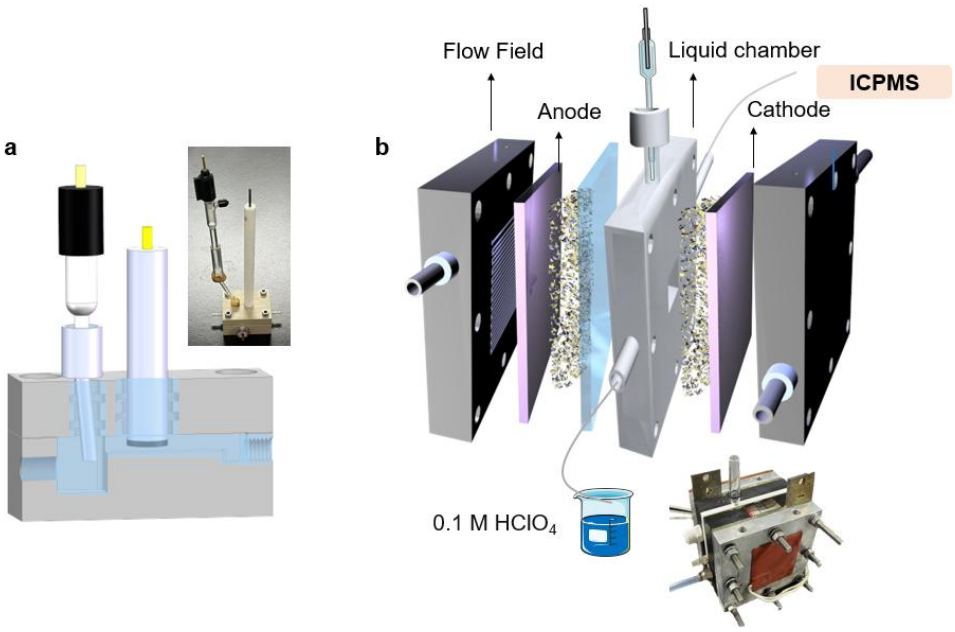

Supplementary Fig. 14. Diagrams of *on-line* ICP-MS device. a, *On-line* ICP-MS equipment on the RDE level. **b,** *On-line* ICP-MS equipment on the GDE level. The *online* ICP-MS measurement setup is similar to that of EPR, except that DMPO is not introduced into the electrolyte.

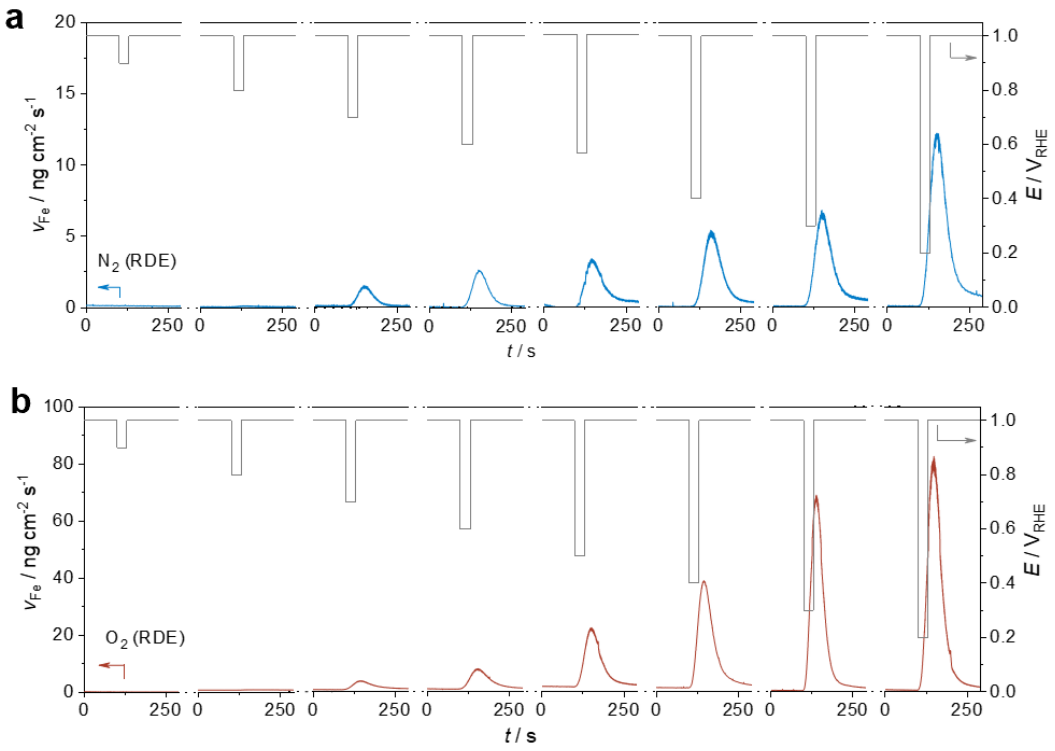

Supplementary Fig. 15. *On-line* Fe dissolution tests in RDE. Tracking of Fe dissolution rate at different electrode potentials from 0.9 to 0.2 V_{RHE} under **a**, N_2 and **b**, O_2 atmospheres.

Under N_2 atmosphere in the RDE, Fe dissolution initiated at 0.8 V_{RHE}, exhibiting a monotonic increase with decreasing potential. When switching to an O_2 atmosphere, a substantial enhancement in Fe dissolution was observed, but maintaining the same monotonically potential-dependent trend.

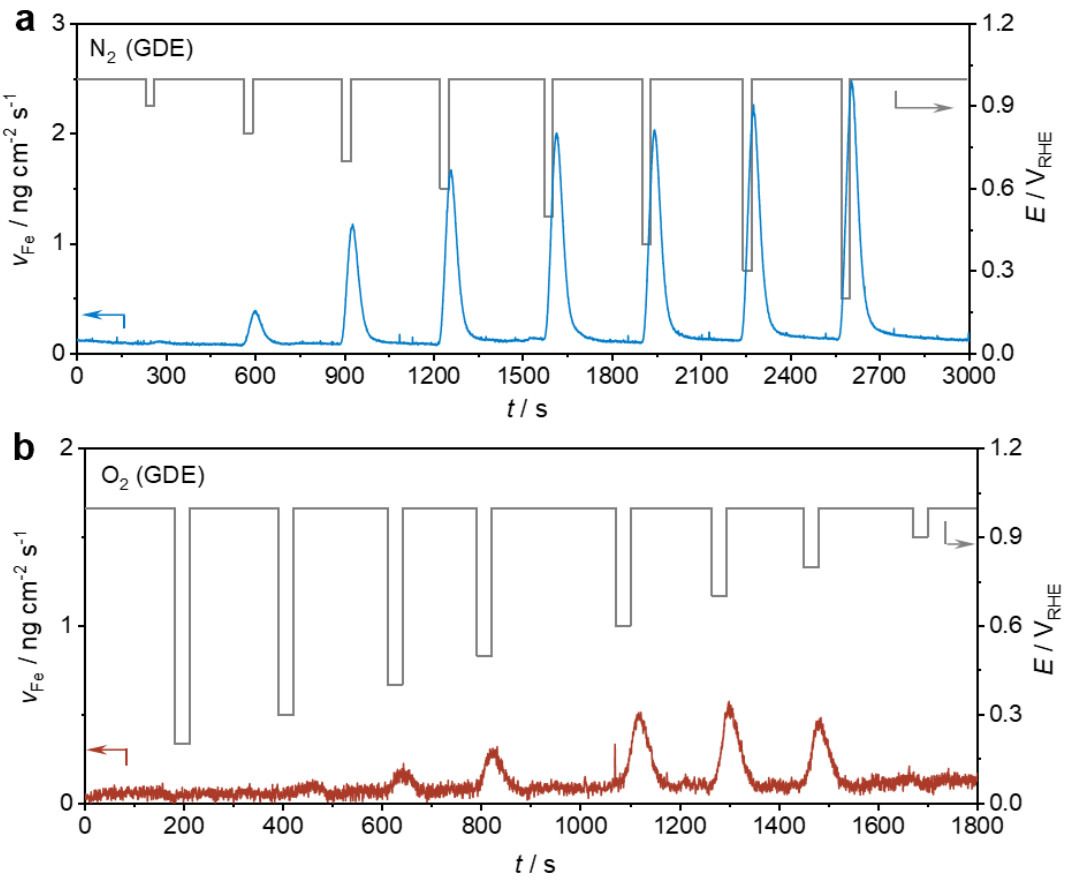

Supplementary Fig. 16. *On-line* Fe dissolution tests in GDE. Tracking of Fe dissolution rate at different electrode potentials from 0.9 to 0.2 V_{RHE} under **a**, N_2 and **b**, O_2 atmospheres.

Under N_2 atmosphere, Fe dissolution increased progressively with decreasing potential, mirroring the behavior observed in the RDE. However, upon introduction of O_2, Fe dissolution showed an increase up to 0.7 V_{RHE}, followed by a stepwise decrease. Below 0.7 V_{RHE}, O_2 conditions showed substantially less dissolution than N_2.

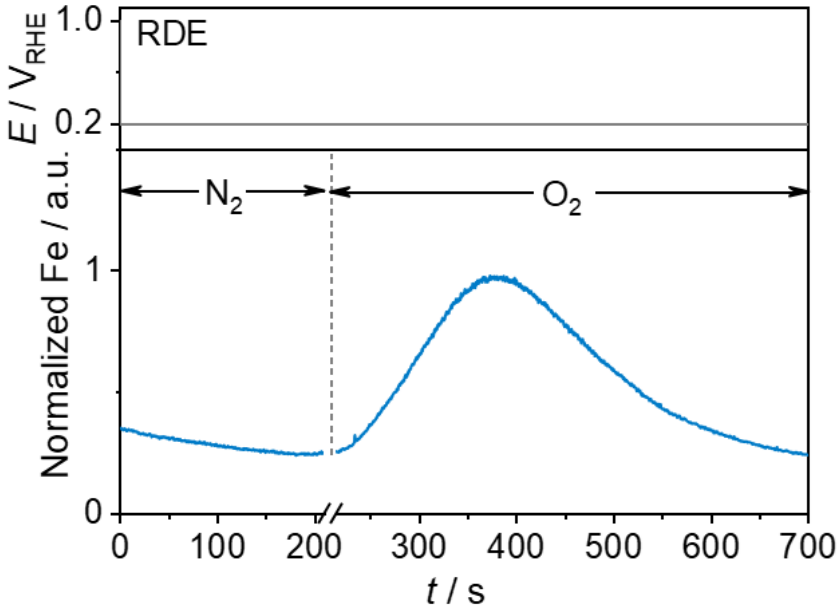

Supplementary Fig. 17. Fe dissolution upon gas switching in RDE. Tracking of Fe dissolution rate during the switch of N_2 to O_2 atmosphere at a constant potential of 0.2 V_{RHE}. After the dissolution curve under N_2 had stabilized, the gas was switched to O_2. All dissolution rates were normalized to their maximum value.

At a constant potential of 0.2 V_{RHE}, the switch of N_2 to O_2 atmosphere results in a rise in Fe dissolution, proving that the ORR accelerates the Fe dissolution.

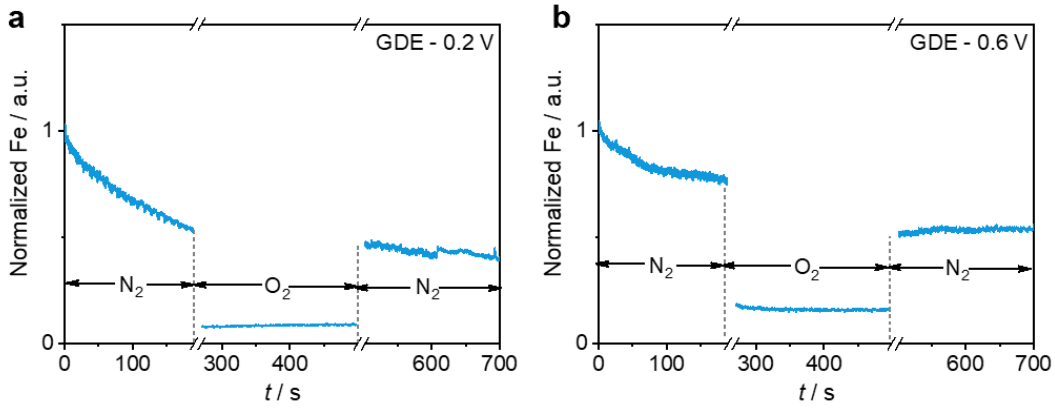

Supplementary Fig. 18. Fe dissolution during gas switching in GDE. Real-time tracking of the Fe dissolution rate during sequential gas switching between O_2 and N_2 at a constant electrode potential of **a**, 0.2 and **b**, 0.6 V_{RHE}. All dissolution rates were normalized to their initial values at t = 0s.

At both 0.6 V and 0.2 V, switching from N_2 to O_2 resulted in a decrease in dissolution, while a subsequent switch back to N_2 led to an increase in dissolution.

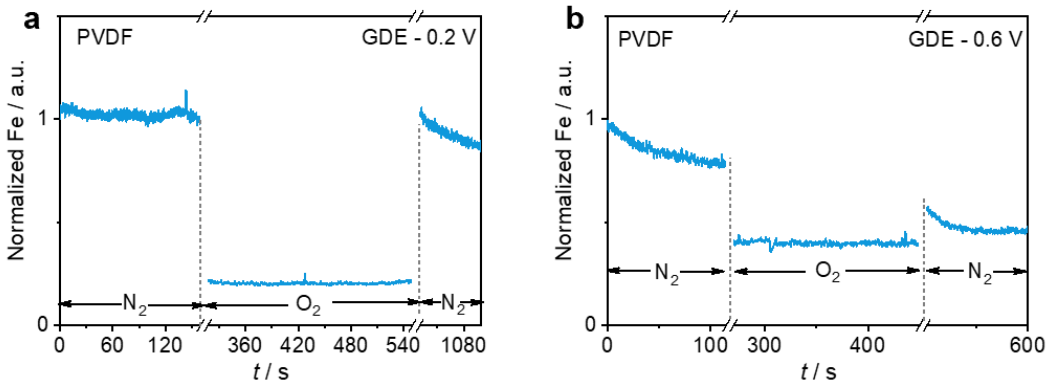

Supplementary Fig. 19. Fe dissolution with PVDF as the binder in GDE. Real-time tracking of the Fe dissolution rate during sequential gas switching between O_2 and N_2 at a constant electrode potential of **a,** 0.2 and **b,** 0.6 V_{RHE}. All dissolution rates were normalized to their initial values at t = 0s.

When Nafion was replaced with PVDF, the inhibitory effect of ORR on dissolution persisted.

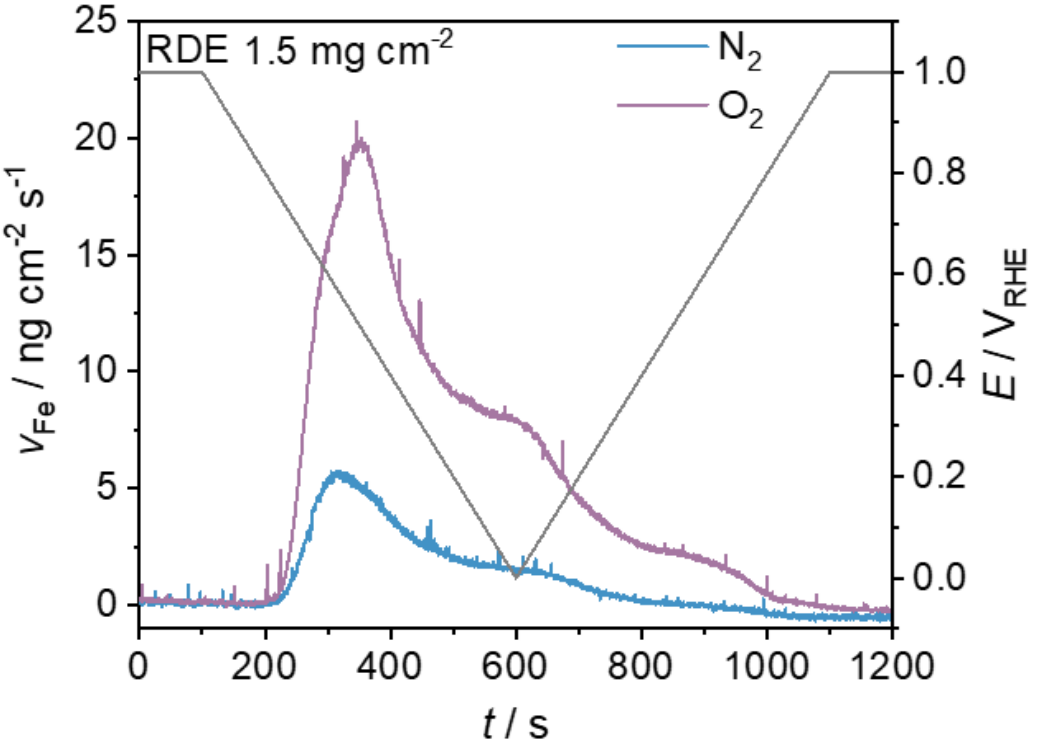

Supplementary Fig. 20. Fe dissolution at a higher catalyst loading on RDE. *Real-time* Fe dissolution curves recorded in both N_2 and O_2 atmospheres at a higher catalyst loading of 1.5 mg cm^{-2}.

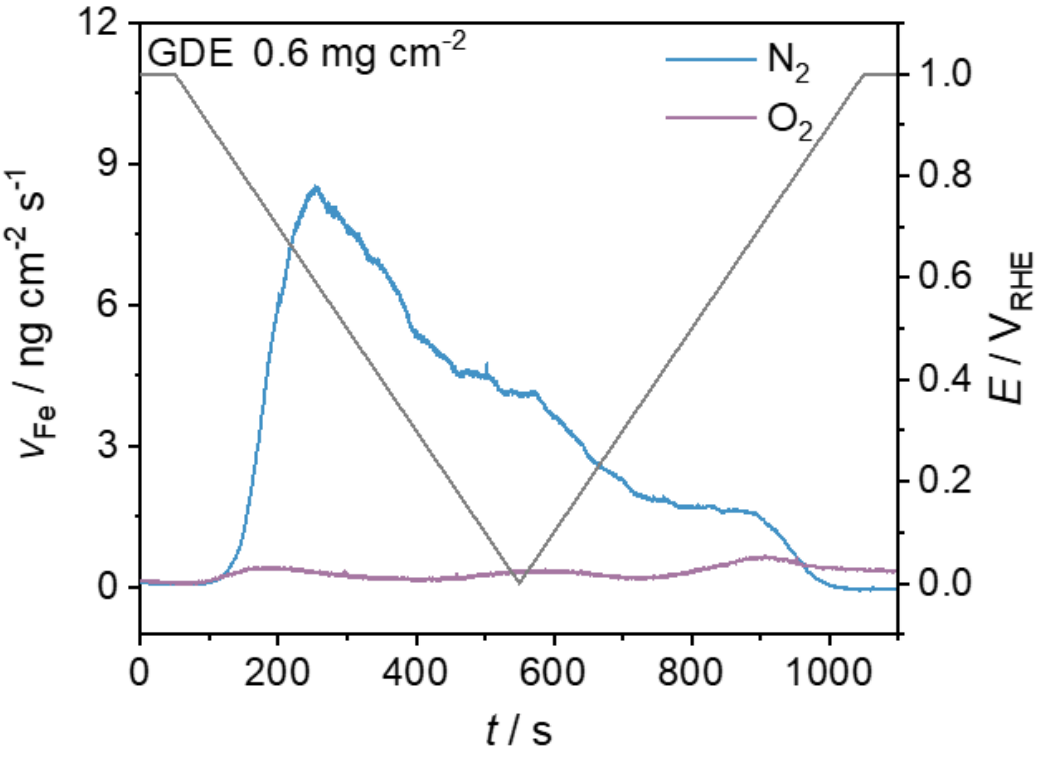

Supplementary Fig. 21. Fe dissolution at a lower catalyst loading on GDE. *Real-time* Fe dissolution curves recorded in both N_2 and O_2 atmospheres at a lower catalyst loading of 0.6 mg cm^{-2}.

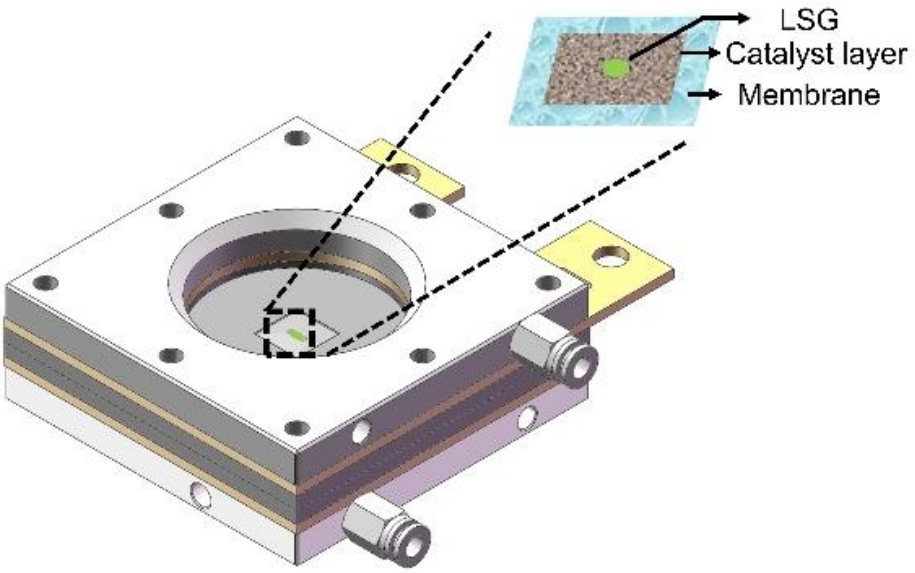

Supplementary Fig. 22. Schematic diagram of *operando* fluorescence device. The graphite plate was windowed and sealed with a quartz window to simultaneously maintain gas tightness and the integrity of the flow field. To probe the pH response, fluorescent probe molecules were incorporated into the catalyst layer.

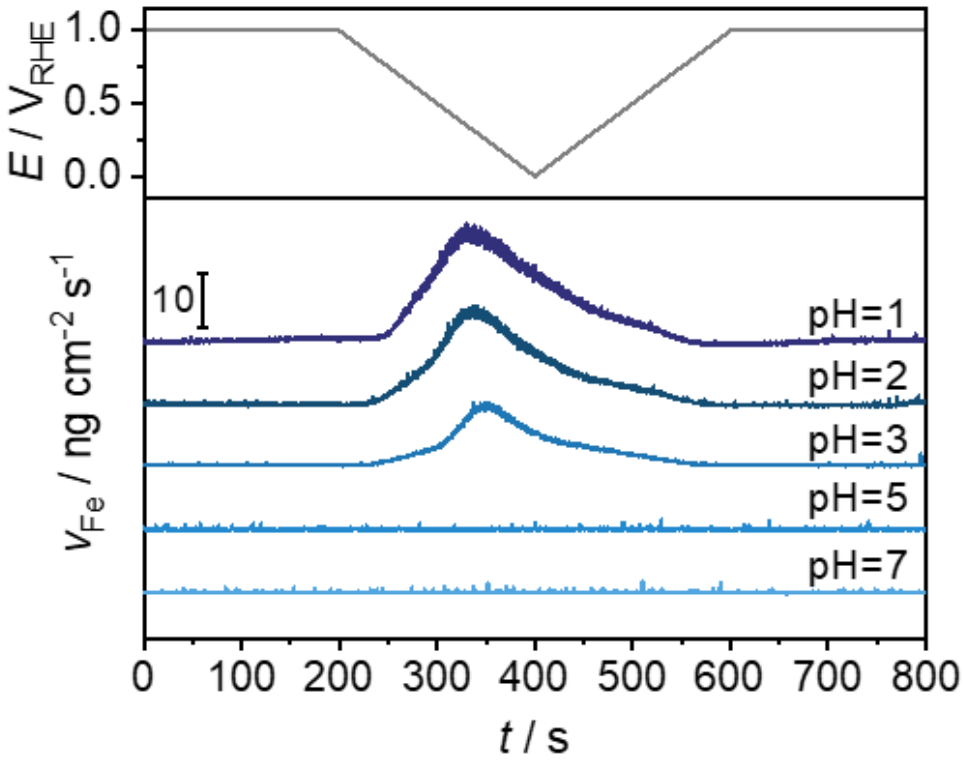

Supplementary Fig. 23. pH-dependent Fe dissolution behavior. Real-time Fe dissolution profiles at five different pH values. The CV protocol consisted of: (i) an initial potentiostatic hold at 1.0 V_{RHE} for 200 s to establish a stable baseline; (ii) one CV cycle between 1.0 V_{RHE} and 0 V_{RHE} at a scan rate of 5 mV s^{-1}; and (iii) a final recovery period at 1.0 V_{RHE} for 200 s.

Fe dissolution decreases with increasing pH. When the pH reaches 5, no significant Fe dissolution signal is observed anymore.

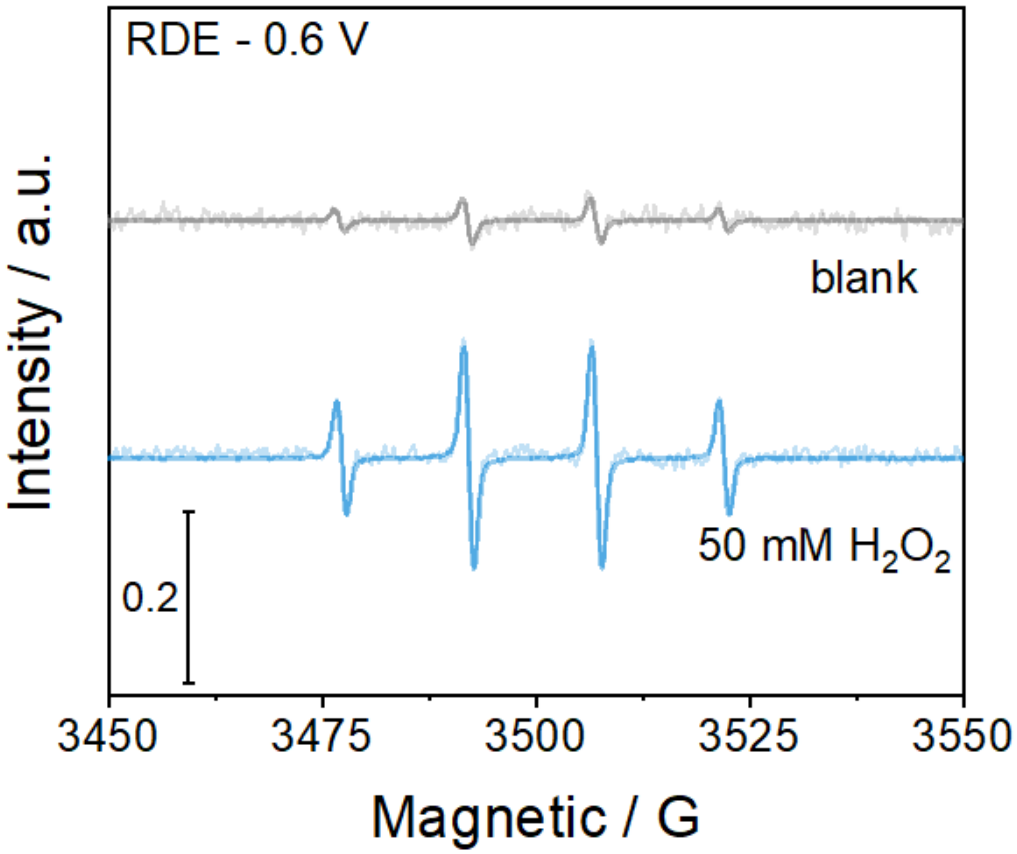

Supplementary Fig. 24. *On-line* EPR tests during H_2O_2RR. *On-line* EPR experiments under RDE before and after the addition of 50 mM H_2O_2 at a constant potential of 0.6 V_{RHE} in a N_2 atmosphere. The radical concentration was measured at 0.6 V_{RHE} with a catalyst loading of 0.6 mg cm^{-2}. Blank measurements were performed using 0.1 M $HClO_4$ solution containing 3 vol% DMPO as a radical scavenger. In the hydrogen peroxide experiment, H_2O_2 was additionally added to the above solution to a concentration of 50 mM. The volumetric flow rate was maintained at 1.5 mL min^{-1} at 25 ºC.

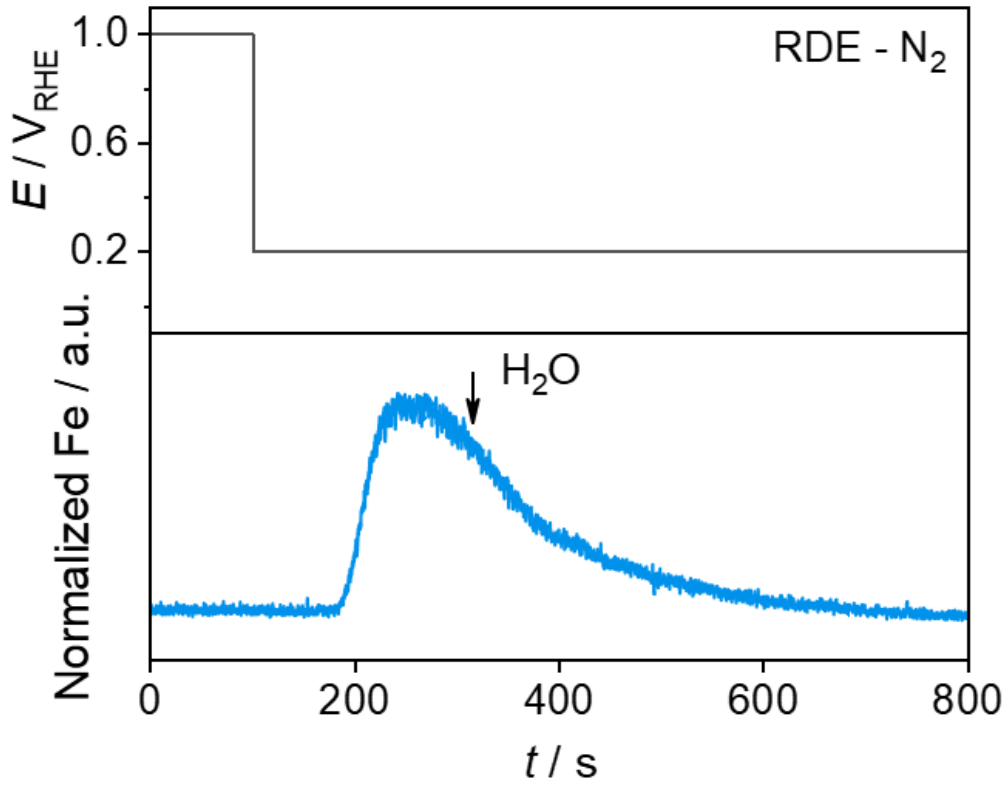

Supplementary Fig. 25. Exclusion of electrolyte dilution effects on Fe dissolution. Real-time monitoring of the Fe dissolution rate using an RDE-based online ICP-MS device. The experiment was conducted at a constant potential of 0.2 V_{RHE} in an N_2 atmosphere.

The injection of ultrapure water (with a volume equal to that of the H_2O_2 solution used in comparative experiments) caused no discernible fluctuation in the dissolution curve, indicating that dilution effects are negligible.

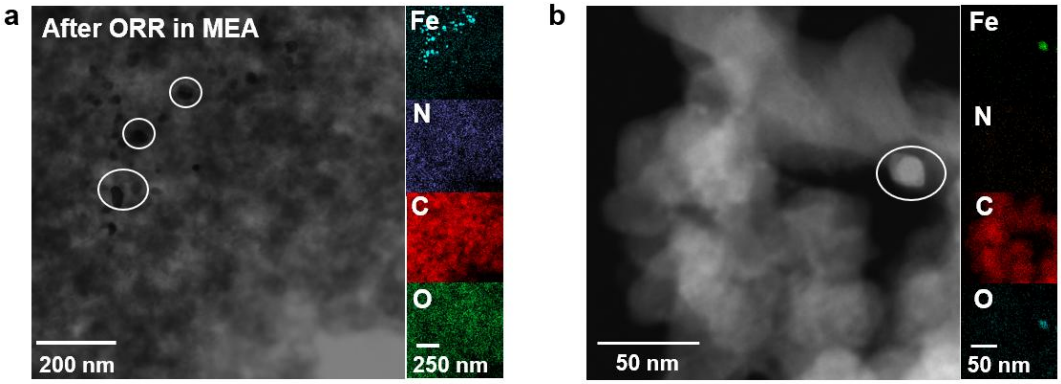

Supplementary Fig. 26. Post-ORR catalyst characterization. TEM images and corresponding elemental maps acquired from different regions of the catalyst, after sequential ORR testing in a GDE and an MEA.

Following operation in a GDE and subsequently in an MEA, representative TEM images and elemental mapping reveal the formation of Fe-rich clusters.

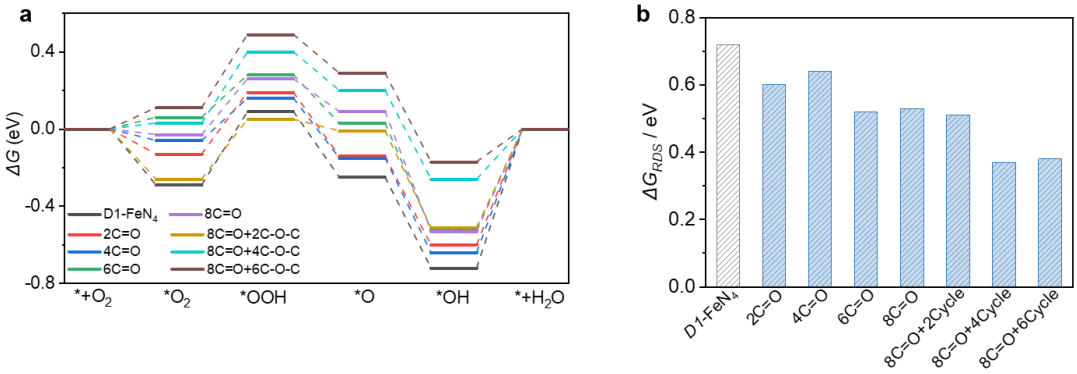

Supplementary Fig. 27. ORR pathways. a, multi-step reaction path free energy step diagram of eight structures. **b,** Gibbs free energy diagrams of RDS with eight structures.

For the 8C=O+6C-O-C and 8C=O+4C-O-C configurations, the RDS is identified as the transformation from *O_2 to *OOH. While for the remaining structural motifs, the RDS shifts to the final protonation step from *OH to *+H_2O.

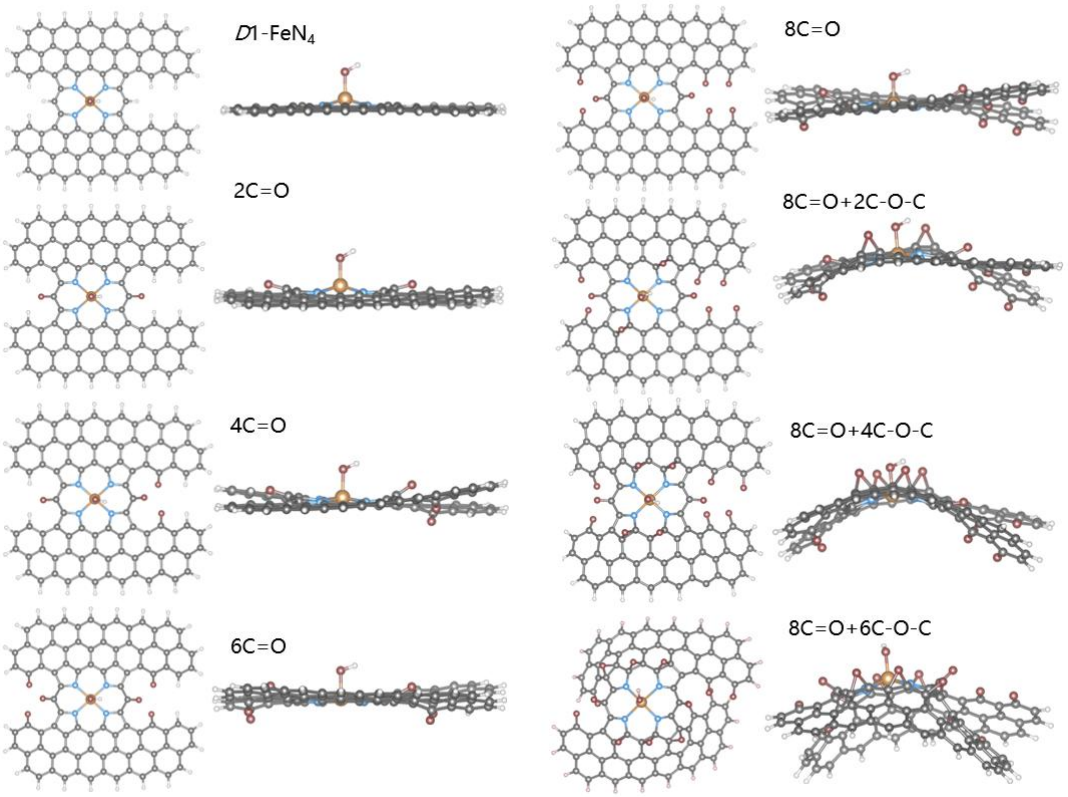

Supplementary Fig. 28. Deformation structure diagram of carbon layers with different oxidation levels.

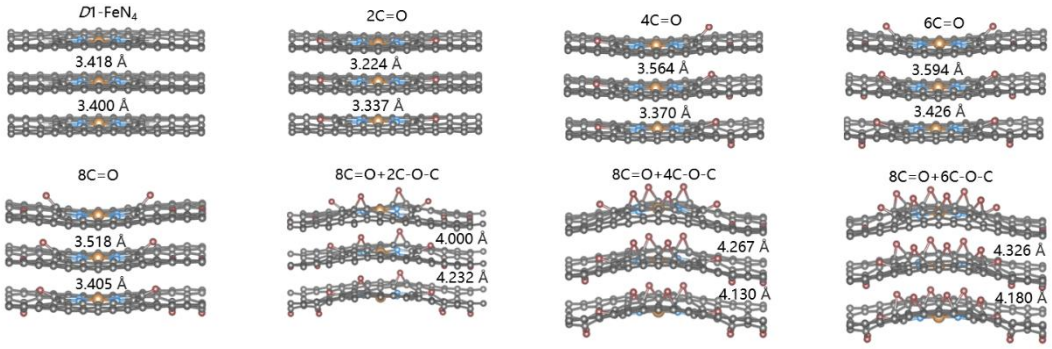

Supplementary Fig. 29. Interlayer spacing diagram of eight structures with different oxidation levels.

Supplementary Table 1. Results of the fitting of the 298 K Mössbauer spectrum of pristine *D*1-Fe/N/C powder, pristine GDE and after ORR GDE, as well as pristine GDE (77 K), after ORR GDE (77 K) and after ORR GDE (8 K): relative area (RA, %), isomer shift (IS), quadrupole splitting (QS), and line width (LW) of each component.

^{57}Fe Samples	Assignment	State	*IS* (mm s^{-1})	*QS* (mm s^{-1})	LW (mm s^{-1})	RA (%)*	X^2
Pristine (Powder 298 K)	*D*1	*S*=5/2	0.34	0.85	0.70	82	689 (1.35)
	*D*2	*S*=0 or 1	0.32	2.46	1.09	11	
	*D*3	*S*=2	1.12	2.98	0.85	7	
Pristine (GDE 298 K)	*D*1	*S*=5/2	0.34	0.85	0.70	82	664 (1.30)
	*D*2	*S*=0 or 1	0.32	2.46	1.09	11	
	*D*3	*S*=2	1.12	2.98	0.85	7	
After ORR (GDE 298 K)	*D*1	*S*=5/2	0.34	0.85	0.70	12	536 (1.06)
	*D*2	*S*=0 or 1	0.32	2.46	1.09	13	
	*D*3	*S*=2	1.12	2.98	0.85	8	
	D4		0.23	1.15	0.98	67	
Pristine (GDE 77 K)	*D*1	*S*=5/2	0.36	0.85	1.99	82	516 (2.03)
	*D*2	*S*=0 or 1	0.33	2.46	1.14	11	
	*D*3	*S*=2	1.13	2.98	2.61	7	
After ORR (GDE 77 K)	*D*1	*S*=5/2	0.34	0.85	2.14	12	284 (1.1)
	*D*2	*S*=0 or 1	0.32	2.46	1.13	13	
	*D*3	*S*=2	1.12	2.98	2.62	8	
	D4		0.25	1.15	2.00	67	
After ORR (GDE 8 K)	*D*1	*S*=5/2	0.34	0.85	2.14	12	630 (1.23)
	*D*2	*S*=0 or 1	0.32	2.46	1.13	13	
	*D*3	*S*=2	1.12	2.98	2.62	8	
	D4		0.25	1.15	2.00	67	

*After ORR, the Fe content in the cathode was determined to be 84% of the pristine value.

Supplementary Table 2. Element contents for Nafion, pristine and after ORR.

	Pristine / at%	**After ORR / at%**
C	84	80
N	5* (5.0)	5* (4.8)
O	11	15

*Perform approximation according to the rounding rule.

Supplementary Table 3. Summary of O1s XPS fitting parameters.

Nafion	Binding energy / eV	FWHM	Area	Atomic / %
SO_3^-	532.8	2.3	29950.6	41.4
CF_2-O-CF_2	535.2	2.1	42392	58.6
Pristine	Binding energy / eV	FWHM	Area	Atomic / %
C=O	531.1	1.9	16420.6	27
C-O	532	1.9	6023.4	10
SO_3^-	532.6	2.1	15544.4	26
CF_2-O-CF_2	534.7	2.0	21762.0	37
After ORR	Binding energy / eV	FWHM	Area	Atomic / %
C=O	531.3	1.9	38538.5	42
C-O	532.2	1.9	16500.6	18
SO_3^-	532.6	2.1	15544.4	17
CF_2-O-CF_2	534.7	2.0	21762.0	23

To ensure fitting accuracy, the two peaks originating from Nafion were maintained at a fixed relative intensity across all samples.

Because the contribution of N-O species to the total O signal is negligible compared with that of C-O and C=O species, no N-O component was included in the O 1s spectral fitting.

Supplementary References

1. Sadezky, A., Muckenhuber, H., Grothe, H., Niessner, R. & Pöschl, U. Raman micro spectroscopy of soot and related carbonaceous materials: spectral analysis and structural information. *Carbon* **43**, 1731-1742 (2005).
2. Wang, K. *et al.* In situ S-doping strategy of promoting iron coordinated by nitrogen-doped carbon nanosheets for efficient oxygen reduction reaction. *ACS Appl. Mater. Interfaces* **14**, 46548-46561 (2022).
3. Pan, Y. *et al.* Regulating the coordination structure of single-atom Fe-NxCy catalytic sites for benzene oxidation. *Nat. Commun.* **10**, 4290 (2019).
4. Vall-llosera, G. *et al.* The C 1s and N 1s near edge X-ray absorption fine structure spectra of five azabenzenes in the gas phase. *J. Chem. Phys.* **128**, 044316 (2008).
5. Hellgren, N. *et al.* Nitrogen bonding structure in carbon nitride thin films studied by soft X-ray spectroscopy. *Appl. Phys. Lett.* **79**, 4348-4350 (2001).
6. Zhao, L. *et al.* Cascade anchoring strategy for general mass production of high-loading single-atomic metal-nitrogen catalysts. *Nat. Commun.* **10**, 1278 (2019).
7. Buettner, G.R. Spin trapping-electron-spin-resonance parameters of spin adducts. *Free Radical Biol. Med.* **3**, 259-303 (1987).
8. Finkelstein, E., Rosen, G.M. & Rauckman, E.J. Spin trapping of superoxide and hydroxyl radical - practical aspects. *Arch. Biochem. Biophys.* **200**, 1-16 (1980).
9. Wang, L.X. *et al.* A polymer tethering strategy to achieve high metal loading on catalysts for Fenton reactions. *Nat. Commun.* **14**, 7841 (2023).